





Communication

Plasma Engineering of Co₄N/CoN Heterostructure for Boosting Supercapacitor Performance

Hong Li ¹, Yunzhe Ma ¹, Xulei Zhang ², Xiuling Zhang ¹ and Lanbo Di ^{1,3,4,*}

¹ College of Physical Science and Technology, Dalian University, Dalian 116622, China; lihong10@dlu.edu.cn (H.L.); myz19981028@163.com (Y.M.); xiulz@sina.com (X.Z.)

² Sunstone Energy Co., Ltd., Jiayuguan 735100, China; xulei951105@163.com

³ State Key Laboratory of Structural Analysis for Industrial Equipment, Dalian University of Technology, Dalian 116024, China

⁴ Key Laboratory of Advanced Technology for Aerospace Vehicles of Liaoning Province, Dalian University of Technology, Dalian 116024, China

* Correspondence: dilanbo@163.com

Abstract: Supercapacitor electrode materials play a decisive role in charge storage and significantly affect the cost and capacitive performance of the final device. Engineering of the heterostructure of metal–organic framework (MOF)-derived transition metal nitrides (TMNs) can be conducive to excellent electrochemical performance owing to the synergistic effect, optimized charge transport/mass transfer properties, and high electrical conductivity. In this study, a Co₄N/CoN heterostructure was incorporated into a nitrogen-doped support by radio-frequency (RF) plasma after simple pyrolysis of Co-based formate frameworks (Co-MFFs), with the framework structure well retained. Plasma engineering can effectively increase the ratio of Co₄N in the Co₄N/CoN heterostructure, accelerating the electron transfer rate and resulting in a rough surface due to the reduction effect of high-energy electrons and the etching effect of ions. Benefiting from the plasma modification, the obtained electrode material Co₄N/CoN@C-P exhibits a high specific capacitance of 346.2 F·g⁻¹ at a current density of 1 A·g⁻¹, approximately 1.7 times that of CoN/Co₄N@C prepared by pyrolysis. The specific capacitance of Co₄N/CoN@C-P reaches 335.6 F·g⁻¹ at 10 A·g⁻¹, approximately 96.9% of that at 1 A·g⁻¹, indicating remarkable rate capability. Additionally, the capacitance retention remains at 100% even after 1000 cycles, suggesting excellent cycling stability. The rational design and plasma engineering of the TMN heterostructures at the nanoscale are responsible for the excellent electrochemical performance of this novel composite material.

Keywords: supercapacitor electrode materials; metal–organic frameworks; transition metal nitrides; Co₄N/CoN heterostructure



Citation: Li, H.; Ma, Y.; Zhang, X.; Zhang, X.; Di, L. Plasma Engineering of Co₄N/CoN Heterostructure for Boosting Supercapacitor Performance. *Materials* **2024**, *17*, 3529. <https://doi.org/10.3390/ma17143529>

Academic Editors: Sergei A. Kulich, Valery A. Svetlichnyi, Aleksandr Kuchmizhak and Mitsuhiko Honda

Received: 15 June 2024

Revised: 9 July 2024

Accepted: 15 July 2024

Published: 16 July 2024



Copyright: © 2024 by the authors. Licensee MDPI, Basel, Switzerland. This article is an open access article distributed under the terms and conditions of the Creative Commons Attribution (CC BY) license (<https://creativecommons.org/licenses/by/4.0/>).

1. Introduction

With the rapid development of renewable and clean energy sources, energy storage systems play a significant role worldwide, particularly in the ever-increasing use of solar and wind energy systems [1–4]. Electrochemical supercapacitors (SCs) as energy storage devices have garnered considerable attention because of their rapid power delivery and recharging with high power density, stability, adaptability to harsh environments, and safety [5,6]. However, some challenges remain, such as their low energy density and high cost, severely limiting their further application [7,8]. Considering that the construction of electrode materials is a key aspect of supercapacitors for enhancing their performance, developing advanced composite materials with cost efficiency using multiple technologies is highly desirable [9–11].

Metal–organic frameworks (MOFs) are a class of novel crystalline porous materials with controllable compositions, diverse structures, and high specific surface areas. MOFs can be converted into porous carbon materials through a simple pyrolysis treatment, making

them widely applicable in energy storage applications [12,13]. MOF-derived porous carbon materials have a porous structure and large specific surface area. Simultaneously, when using Zn-, Fe-, and Co-based MOFs as electrodes for supercapacitors, the presence of metal centers may enhance their ability to store energy through pseudocapacitance [14–16]. These remarkable structural advantages enable the great potential of MOF-derived carbon as high-performance energy materials, which, to date, have been applied in the field of energy storage systems. However, their relatively low specific capacitances limit their practical applications [17–19]. In recent years, considerable effort has focused on transition metal nitrides (TMNs) (especially Co_4N) and their diverse compositions owing to their excellent electrical conductivity, chemical corrosion resistance, chemical reactivity, and electrochemical stability [20–22]. Typically, TMNs contain metallic, ionic, and covalent bonds. Metal–nitride bonding expands the parent metal lattice and narrows its d-bands [5,23–25]. Owing to the scarcity of the d-band and increased density of states (DOS) near the Fermi level of TMNs, they display characteristics similar to those of noble metals in electrocatalysis, which enables them to effectively attract reactants/ions to their surfaces, thus making them appealing options for electrochemical energy storage and conversion [26,27]. Therefore, maximizing the overall electrochemical performance by carefully integrating the advantages of the Co_xN and MOF structures by exploiting the intrinsic characteristics of different materials is beneficial.

Recently, significant progress has been made in heterostructure engineering, a highly effective approach for achieving optimal control over electrochemical activity and mass and charge transport. The advantages of heterostructures can be primarily attributed to synergistic effects, strain effects, and electronic interactions [28]. The synergistic effect, one of the most important characteristics of heterostructures, is induced by heterointerfaces and multiple components. In general, the interfacial bonding in these heterostructures can effectively facilitate electron transfer and enhance electrical conductivity. In addition to conductivity, other qualities, such as hydrophilicity, the density of active sites, electrochemical stability, mechanical properties, and mass-transfer efficiency, can be adjusted [29]. Moreover, owing to their diverse chemical compositions and crystal structures, the arrangement of atoms at the heterointerface differs from that in bulk materials, causing lattice strain, including both tensile and compressive strains. Typically, heterostructures subjected to tensile strain cause a decrease in the overlap of the d-orbitals, reducing the bandwidth, which, in turn, causes an increase in the d-band center and enhances the adsorption energy [30]. Finally, heterostructured materials inevitably alter the electronic structure in each phase along their interfaces—beneficial for electronic interactions and surface electron modulation [31,32]. Therefore, modifying heterostructures through chemical/physical methods can further optimize the electronic structure and charge transport/mass transfer properties in the electrochemical process and enhance the capacitive performance.

Cold plasma is a rapid, facile, and environmentally friendly method for treating different materials, and it has consequently garnered growing research interest [33–35]. Among the diverse plasmas, radio-frequency (RF) plasma can generate abundant high-energy electrons, ions, and active species at low pressures with a low gas temperature and precisely induce nanoscale reactions in electrode materials, achieving reduction, doping, etching, and exfoliation [33]. For a typical argon ICP discharge, the high-energy electrons present in the plasma can realize the reduction of cobalt ions to a lower valence, while the ions with high energy can etch the material surface by physical bombardment, making the surface structure rougher, exposing more Co_xN active sites, and promoting the formation of heterostructures [36,37]. Additionally, a low gas temperature is beneficial for preventing structural damage to the MOFs and particle agglomeration.

Based on the above understanding, this study utilizes a plasma modification strategy to regulate the contents of $\text{Co}_4\text{N}/\text{CoN}$ heterostructures and the surface morphology of MOF materials, resulting in a $\text{Co}_4\text{N}/\text{CoN}@C\text{-P}$ material. This material combines the advantages of porous MOFs and N-doped carbon structures, with the $\text{Co}_4\text{N}/\text{CoN}$ heterostructure accelerating the charge transfer between the crystal interface, enhancing the electrical

conductivity. Thus, the obtained Co₄N/CoN@C-P exhibits excellent electrochemical performance in supercapacitors.

2. Experimental Section

2.1. Preparation of the Electrode Materials

2.1.1. Preparation of Co-MFF

Co-MFFs were prepared using the liquid-phase precipitation method. The basic process was as follows: First, 0.58 g of cobalt nitrate and 0.5 g of polyethylene glycol (PEG) were weighed and dissolved in 10 mL methanol; the dissolved solution is denoted as solution A. Then, 1.01 g of ammonium formate and 0.5 g of PEG were weighed and dissolved in 10 mL methanol to obtain solution B; solution B was stirred at a constant speed. After all solids in solution B were dissolved, solution A was slowly added dropwise to solution B. After continuous magnetic stirring at room temperature for 1 h, a pink solid powder was separated after 24 h, centrifuged with ethanol five times, and dried in a vacuum drying oven at 55 °C for 7 h to obtain the Co-MFF sample [38].

2.1.2. Preparation of CoN/Co₄N@C

A Co-MFF sample (2 g) was pyrolyzed in a tube furnace. An ammonia/argon gas mixture ($V_{\text{NH}_3}:V_{\text{Ar}} = 1:9$) was utilized, with a total flow rate of 50 mL·min⁻¹, pyrolysis temperature of 450 °C, heating rate of 5 °C·min⁻¹, and pyrolysis time of 2 h. After pyrolysis and natural cooling to room temperature, the sample was collected, weighed, and labeled as CoN/Co₄N@C.

2.1.3. Preparation of Co₄N/CoN@C-P

A CoN/Co₄N@C sample (400 mg) was treated in a low-pressure radio frequency (RF)-based inductively coupled plasma (ICP) setup. After the chamber vacuum was pumped to 0.1 Pa, argon (or nitrogen) was fed into the chamber for 20 min, the RF automatic impedance matcher and RF power supply were turned on, the CoN/Co₄N@C was processed at a gas pressure range of 20–60 Pa under RF power of 200–350 W for 2–8 min, and then the RF power was turned off. When the quartz tube decreased to room temperature, the sample was collected, weighed, and labeled as Co₄N/CoN@C-P. It should be noted that the discharge conditions mentioned later in this work refer to argon plasma with 40 Pa, 300 W, and 6 min unless otherwise specified.

2.2. Electrochemical Measurement

Cyclic voltammetry (CV), galvanostatic charge–discharge (GCD), and electrochemical impedance spectroscopy (EIS) were performed using an electrochemical workstation (CHI760E, CH Instruments, China). In the tests, the CV scanning rate was 10–50 mV·s⁻¹ and the GCD current density was 1–10 A·g⁻¹. The EIS tests were performed at a frequency of 0.01–10⁵ Hz with 5 mV AC perturbation. According to the GCD curve, the specific capacitance of the sample can be calculated as

$$C = \frac{I\Delta t}{m\Delta V} \quad (1)$$

where I is the current, Δt is the discharge time, m is the mass of the active substance, and ΔV is the potential difference.

The coulombic efficiency can be calculated as

$$\eta = \frac{\Delta t_d}{\Delta t_c} \quad (2)$$

where η is the coulombic efficiency, and Δt_d and Δt_c are the discharge and charging time, respectively.

2.3. Characterization

The species composition and phase structure of the samples were analyzed by X-ray diffraction (XRD) (DX-2700, Dandong, China), and the diffraction source was a Cu-K α ray operated at a voltage of 40 kV and a current of 30 mA. The morphologies of the samples were investigated using scanning electron microscopy (SEM) (ZEISS Gemini 300, Jena, Germany) at an accelerating voltage of 5 kV. High-resolution transmission electron microscopy (HRTEM) (Talos Model F200X, Waltham, MA, USA) was used to observe the morphologies of the samples at an accelerating voltage of 120 kV. The surface chemistry valence states of the composites were analyzed by XPS (Thermo Scientific Model K-Alpha, Waltham, MA, USA). The excitation source was an X-ray source with a monochromatic Al target (photon energy of 1486.6 eV, 150 W), with C1s (binding energy = 284.8 eV) used to correct the displacement of each element in the test during the analysis.

3. Results and Discussion

3.1. Electrochemical Performance

At 300 W and 40 Pa, the Co₄N/CoN@C-P samples treated by argon RF ICP for 6 min exhibited the best performance (Figures S2–S4). Co-MFF, CoN/Co₄N@C, and Co₄N/CoN@C-P were fabricated into electrode sheets, and their electrochemical performance was measured in a 6 M KOH electrolyte using a three-electrode system. Figure 1a shows the CV curves of Co-MFF, CoN/Co₄N@C, and Co₄N/CoN@C-P at a scan rate of 10 mV·s⁻¹ and a voltage range of 0–0.35 V. Co₄N/CoN@C-P exhibited a higher capacitive current response and a larger CV integration area, implying a larger charge storage capacity. Figure 1b shows the GCD curves of the three electrode materials at a current density of 1 A·g⁻¹ and a voltage range of 0–0.35 V. Compared to the Co-MFF and CoN/Co₄N@C, Co₄N/CoN@C-P had longer charge/discharge times, consistent with the trend of the CV curves. Moreover, the specific capacitance of Co₄N/CoN@C-P was 346.2 F·g⁻¹, much higher than that of CoN/Co₄N@C (208.5 F·g⁻¹) under the same conditions. Figure 1c shows the EIS results for the three electrode materials, with the upper inset showing the equivalent circuit diagram and the lower inset showing the local enlarged image. The fitted Nyquist plots of Co-MFF, CoN/Co₄N@C, and Co₄N/CoN@C-P are composed of a semicircular arc and a straight line. The semicircular arc observed in the high-frequency region represents the redox reaction occurring at the interface between the electrode and the electrolyte. The straight line observed in the low-frequency region indicates the diffusion of ions in the electrode. An equivalent circuit was established to better interpret the Nyquist plots (upper inset in Figure 1c), and all the fitted results are summarized in Table S1. The intersection of the semicircular arc in the high-frequency region and the real axis represents the series resistance (R_s), and the diameter of the semicircular arc represents the charge transfer resistance (R_{ct}). Constant phase element 1 connected in parallel with R_{ct} represents a Faraday capacitor (C_F), and constant phase element 2 connected in series represents an electric double-layer capacitor (C_{dl}). As shown in Table S1, R_s and R_{ct} of Co₄N/CoN@C-P are 0.73 and 0.28 Ω , respectively, which are lower than those of CoN/Co₄N@C ($R_s = 0.73 \Omega$, $R_{ct} = 0.34 \Omega$) and Co-MFF ($R_s = 1.38 \Omega$, $R_{ct} = 0.54 \Omega$). In short, the Co₄N/CoN@C-P material has the largest slope in the low-frequency region and a smaller arc radius in the high-frequency region, indicating that the sample has minimal resistance, which, in turn, indicates that the electrode material has good electrical conductivity—conducive to rapid charge transfer. Figure 1d exhibits the CV curves of Co₄N/CoN@C-P at 10–50 mV·s⁻¹ scan rates. Although the absence of narrow redox peaks is observed, the CV curve shape is not an ideal rectangle, indicating a charge contribution from a pseudocapacitance mechanism [39]. By increasing the scan rate, the redox peaks gradually separate, while the shape of the CV curve remains unchanged, implying faradaic pseudocapacitance behavior, excellent reversibility, and faster charge transfer [39–41]. Generally, capacitance decreases with increasing current density owing to the diffusion effect. However, as shown in the GCD plot of Co₄N/CoN@C-P given in Figure 1e at 1–10 A·g⁻¹, the specific capacitance of Co₄N/CoN@C-P at 10 A·g⁻¹ is approximately 96.9% of that at a current density of 1 A·g⁻¹, indicating excellent energy

storage performance and rate capability. The cyclic stability of $\text{Co}_4\text{N}/\text{CoN}@C\text{-P}$ is also evaluated in the voltage range of 0–0.35 V and a current density of $1 \text{ A}\cdot\text{g}^{-1}$, as shown in Figure 1f. After 1000 cycles, the capacitance retention reached 100%, and the coulombic efficiency was consistently maintained at nearly 100%, indicating excellent cycling stability and a favorably reversible charge storage and delivery process. The improved capacitive performance of $\text{Co}_4\text{N}/\text{CoN}@C\text{-P}$ can be attributed to its unique morphology and structure.

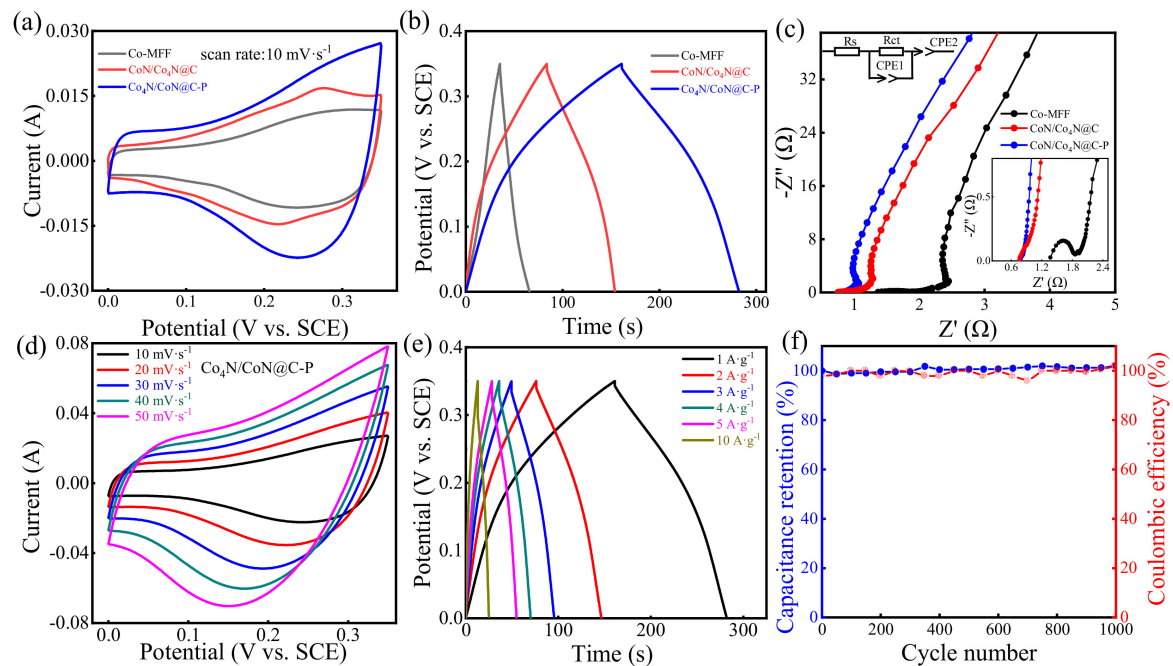


Figure 1. Electrochemical performance of Co-MFF, CoN/Co₄N@C, and Co₄N/CoN@C-P electrodes in 6 M KOH electrolyte with a three-electrode system. (a) CV curves at $10 \text{ mV}\cdot\text{s}^{-1}$; (b) GCD curves at $1 \text{ A}\cdot\text{g}^{-1}$; (c) EIS curves; (d) CV profiles of Co₄N/CoN@C-P at different scan rates; (e) GCD curves of Co₄N/CoN@C-P at different current densities; (f) Capacitance retention and coulombic efficiency of the Co₄N/CoN@C-P over 1000 cycles at $1 \text{ A}\cdot\text{g}^{-1}$.

3.2. Morphological and Structural Characterizations

XRD characterization tests were conducted for Co-MFF, CoN/Co₄N@C, and Co₄N/CoN@C-P, as shown in Figure 2, to investigate the crystal phase structures of the different electrode materials. The positions of the Co-MFF diffraction peaks at $2\theta = 13.97^\circ, 17.69^\circ, 26.66^\circ, 32.81^\circ, 35.81^\circ, 39.14^\circ, 42.77^\circ, 43.76^\circ,$ and 48.47° are consistent with those of Co-MFF in the literature [42,43]. The diffraction peaks of CoN/Co₄N@C at $2\theta = 44.59^\circ, 51.70^\circ,$ and 76.10° correspond to the characteristic diffraction peaks of Co₄N at the (111), (200), and (220) crystal faces (JCPDS: 41-0943) of the cubic phase, respectively. The diffraction peaks at $2\theta = 36.19^\circ, 42.19^\circ,$ and 61.34° correspond to the characteristic diffraction peaks of the (111), (200), and (220) crystal faces (JCPDS: 16-0116) of CoN. The characteristic diffraction peaks of Co₄N and CoN in the cubic phase are also observed in Co₄N/CoN@C-P. Compared to CoN/Co₄N@C, the characteristic peak of Co₄N in Co₄N/CoN@C-P is higher and sharper than that of CoN, indicating that the ratio of Co₄N in Co₄N/CoN@C-P increased after the argon RF plasma treatment. This maybe because the high-energy electrons generated in the plasma have strong reduction ability, and the high-valence state of cobalt ions can be reduced to a lower one.

SEM tests were conducted to further examine the surface morphologies and microstructures of the Co-MFF, CoN/Co₄N@C, and Co₄N/CoN@C-P electrode materials. Figure 3a–c show the surface morphologies of the Co-MFF at different scales. The sample presents an octahedral morphology, signifying the successful synthesis of Co-MFF. Figure 3d–f show the surface morphologies of CoN/Co₄N@C at different scales. The existence of the octahedral morphology and a porous structure indicates that the framework of Co-MFF

was stable after ammonia/argon pyrolysis. The structural confinement effect of the MFF framework helps stabilize the CoN and Co₄N nanoparticles and avoid nanoparticle agglomeration. Figure 3g–i show the surface morphology of Co₄N/CoN@C-P, maintaining the basic morphology of the MFF, with the frame structure still in good condition; however, the surface of the treated sample became rougher because the high-energy argon ions generated in the plasma can strongly physically bombard the surface of the material, causing the surface of the material to be etched. A rough surface topography is usually conducive to full contact between the electrode surface and the electrolyte, facilitating ion mass transfer, reducing the electrolyte diffusion distance, and further improving the capacitance of the electrode material [44].

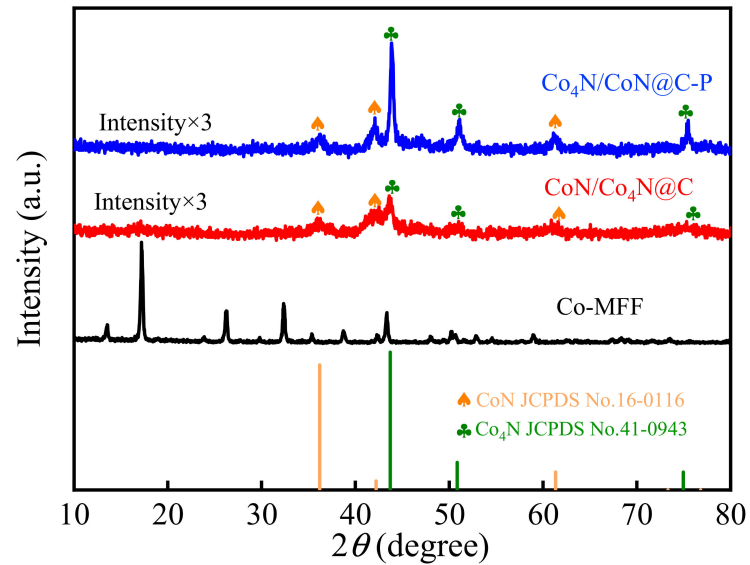


Figure 2. XRD patterns of Co-MFF, CoN/Co₄N@C, and Co₄N/CoN@C-P.

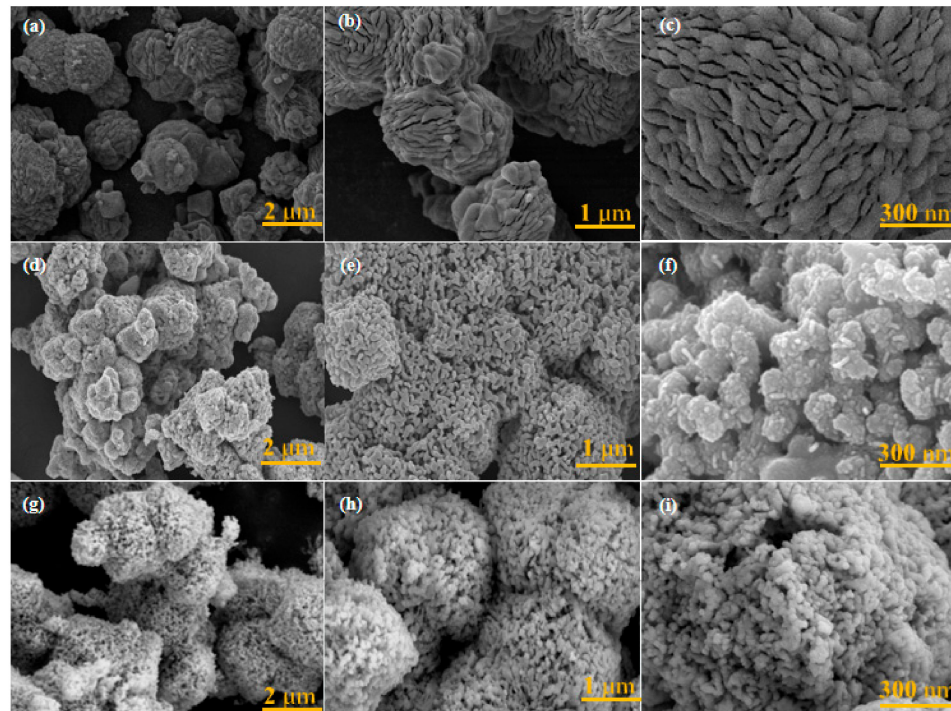


Figure 3. Typical SEM images of (a–c) Co-MFF, (d–f) CoN/Co₄N@C, and (g–i) Co₄N/CoN@C-P.

Clear lattice fringes of 2.48 Å and 2.08 Å, corresponding to the CoN (111) and Co₄N (111) crystal faces, were observed in the HRTEM images of the CoN/Co₄N@C and Co₄N/CoN@C-P (Figure 4a,c), respectively, and exhibited an apparent heterointerface, indicating the formation of the Co₄N and CoN heterostructures in the CoN/Co₄N@C and Co₄N/CoN@C-P. Relevant research results show that the redistribution of electrons at the heterointerface can promote a synergistic effect between Co_xN heterostructures, resulting in a higher electrical conductivity of the heterostructures—conducive to enhancing the electrochemical properties of the prepared electrode materials [45–47]. Indeed, as shown in Figures S1 and S2, the Co₄N@C-P with a single component of Co₄N obtained by treating CoN/Co₄N@C with nitrogen plasma exhibited lower electrochemical performance. In addition, as shown in Figure 4b,d, the energy-dispersive X-ray spectroscopy (EDS) elemental mapping images demonstrate that Co, N, and C were uniformly distributed in the CoN/Co₄N@C and Co₄N/CoN@C-P.

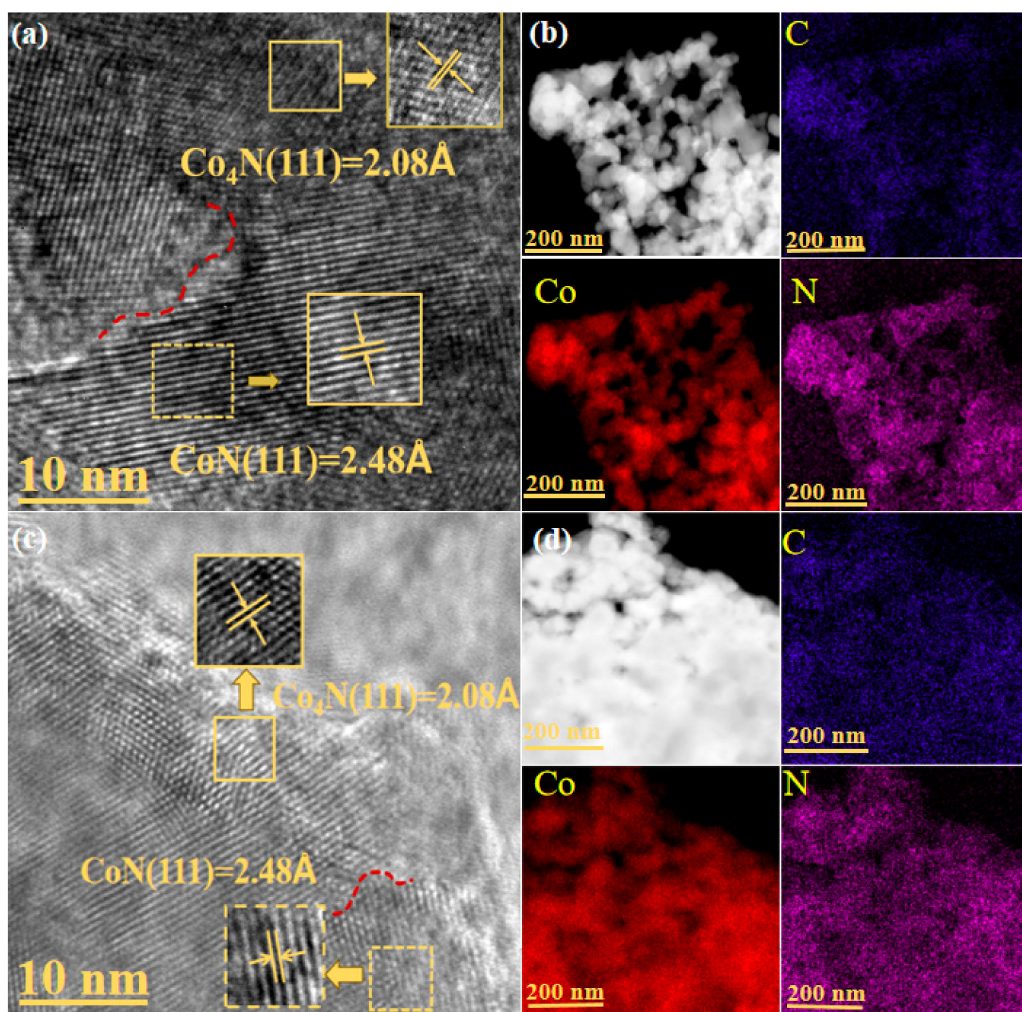


Figure 4. HRTEM images and EDS elemental mappings of the Co, N, and C elements for (a,b) CoN/Co₄N@C and (c,d) Co₄N/CoN@C-P (The red dash lines indicate the heterointerface).

Considering that the plasma-induced surface modification of materials usually affects the electron valence states of surface atoms, the chemical valence states and surface element compositions of the CoN/Co₄N@C and Co₄N/CoN@C-P were examined by XPS. Figure 5 shows the XPS energy spectra of C1s, Co2p, and N1s of the CoN/Co₄N@C and Co₄N/CoN@C-P materials (with C1s 284.8 eV as the standard peak). In Figure 5a (C1s spectra), the peaks at the binding energies of 284.8, 286.3, and 289.1 eV correspond to the convolution peaks of the C=C, C-N, and N-C=O bonds, respectively. The CoN/Co₄N@C and

Co₄N/CoN@C-P had some N doped into the carbon layer structure. However, the increase in the C-N bond peak area in the Co₄N/CoN@C-P compared to that of the CoN/Co₄N@C indicates an increase in the proportion of nitrogen doping. This enhanced nitrogen doping helped improve the polarity of the electrode material, ensuring full contact with the electrolyte, and effectively improving the specific capacitance and conductivity of the electrode material.

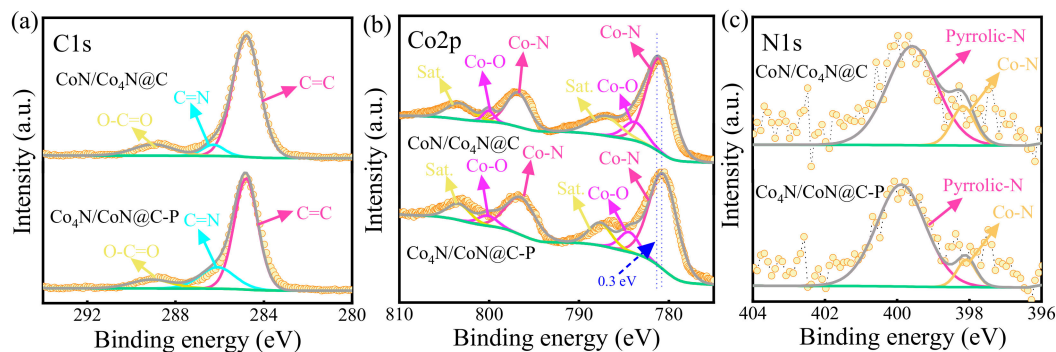


Figure 5. XPS spectra of (a) C1s, (b) Co2p, and (c) N1s for CoN/Co₄N@C and Co₄N/CoN@C-P.

Figure 5b shows the Co2p spectra of the CoN/Co₄N@C and Co₄N/CoN@C-P. The CoN/Co₄N@C signals at 781.1 and 796.8 eV are attributed to the Co-N bond in the CoN compound, while the signals at 787.2 and 803.3 eV are attributed to the Co2p satellite peak. The signals of the Co₄N/CoN@C-P sample at 780.8 and 796.5 eV are attributed to the Co-N bond in the CoN compound, with satellite peaks at 787.6 and 803.6 eV [39]. The two spin-splitting peaks at 784.2 and 801.1 eV may be related to sample surface oxidation [48,49]. Based on a semi-quantitative analysis of the samples, the ratios of Co/C in the CoN/Co₄N@C and Co₄N/CoN@C-P are approximately 1:7.85 and 1:7.68, respectively, indicating that the ratios of Co/C in the samples treated by plasma modification are relatively stable. Combined with the XRD results, the valence state of Co and the relative contents of CoN and Co₄N changed under the effect of plasma reduction. Moreover, compared to the binding energy of the Co-N bond in the CoN/Co₄N@C, the value of the Co₄N/CoN@C-P shifted downward by 0.3 eV, indicating a strong electronic interaction between Co₄N and CoN, eventually resulting in charge redistribution between the heterogeneous interfaces—conductive to the improvement of capacitive performance [50,51].

Figure 5c shows the energy spectra of N1s. The two binding energy peaks of 398.2 and 399.7 eV in the CoN/Co₄N@C are attributed to the Co-N and pyrrole nitrogen peaks, respectively, further confirming the formation of metal nitrides. The binding energy peaks of 398.1 and 399.9 eV in the Co₄N/CoN@C-P correspond to the Co-N and pyrrole nitrogen peaks, respectively. These N dopants help enhance the conductivity of the electrode, promote electron transport performance, and contribute to the additional pseudocapacitance [52–54].

The specific surface area (S_{BET}) of the samples plays a key role in the charge transfer and storage. The BET of the samples was also obtained, as illustrated in Table S2. The S_{BET} of the Co-MFF was $65.0 \text{ m}^2 \cdot \text{g}^{-1}$ in this work. The S_{BET} values of the CoN/Co₄N@C, obtained by the pyrolysis of Co-MFF, and the Co₄N/CoN@C-P, prepared by the plasma processing of CoN/Co₄N@C, were only 17.7 and $7.0 \text{ m}^2 \cdot \text{g}^{-1}$. The S_{BET} value of Co₄N/CoN@C-P was smaller than that of CoN/Co₄N@C. Therefore, it further verifies that the Co₄N/CoN heterostructure instead of the S_{BET} plays a vital role in boosting supercapacitor performance.

3.3. Discussion

In summary, a rapid, simple, and mild plasma surface modification method was employed to treat Co-MFF after simple pyrolysis. This process enables nitrogen doping of the support when constructing and regulating the Co₄N/CoN heterostructure. From the electrochemical performance results of the three materials (Figure 1), the Co₄N/CoN@C-P electrode material prepared by plasma-assisted pyrolysis exhibited superior electrochemical

performance compared to the electrode materials before and after the pyrolysis of Co-MFF, exhibiting a specific capacitance of $346.2 \text{ F}\cdot\text{g}^{-1}$ at a current density of $1 \text{ A}\cdot\text{g}^{-1}$, approximately 1.7 times that of CoN/Co₄N@C prepared by pyrolysis. Furthermore, Co₄N/CoN@C-P demonstrated a remarkable rate capability and excellent cycling stability. The improved capacitive performance of Co₄N/CoN@C-P can be attributed to its optimized heterostructure and the rough surface of the modified MFF structure.

The SEM results indicate that the framework structure of the MFF remained unchanged after RF plasma treatment—beneficial for the dispersion of cobalt–nitrogen nanoparticles. The HRTEM images show the formation of Co₄N and CoN heterostructures in both CoN/Co₄N@C and Co₄N/CoN@C-P. The XRD results reveal that the relative contents of Co₄N and CoN changed significantly after plasma treatment owing to the strong reduction ability of the high-energy electrons generated in the plasma, which generated more Co₄N through its reduction effect. The synergistic effect between the increased Co₄N and CoN heterostructures facilitated a rapid charge transfer during the charge/discharge process, resulting in a higher electrical conductivity of the heterostructures and significantly enhancing the electrochemical performance.

Additionally, the SEM results indicate that the material surface became rougher after the plasma treatment, owing to the etching effect caused by the high-energy argon ions bombarding the material surface in the plasma, which can expose more Co_xN active sites. Furthermore, the porous nature of the MFF material facilitates electron transport, and the etching effect of the plasma promotes the formation of a heterostructure [36]. The XPS results show that plasma surface modification can increase nitrogen doping into the carbon in Co₄N/CoN@C-P, which promotes better contact between the electrode and electrolyte and improves the conductivity of the material, thus enhancing the electrochemical performance of the Co₄N/CoN@C-P electrode material. Finally, the BET results further verify that the Co₄N/CoN heterostructure instead of the S_{BET} plays a vital role in boosting supercapacitor performance.

4. Conclusions

A Co₄N/CoN@C-P electrode material with high electrochemical performance was prepared by an integrated strategy combining plasma modification and the simple pyrolysis of Co-MFF. This approach successfully promoted the nitrogen doping of the carbon support after plasma treatment, formed a Co₄N/CoN heterostructure, and increased the proportion of Co₄N. The electrochemical performance of the electrode materials was measured using a three-electrode system, which revealed that the specific capacitance of Co₄N/CoN@C-P reached up to $346.2 \text{ F}\cdot\text{g}^{-1}$, approximately 1.7 times that of the CoN/Co₄N@C prepared by pyrolysis only. The characterization results indicate that the framework structure of the Co-MFF was well retained after plasma modification—beneficial for the dispersion of cobalt nitride nanoparticles. The porous nature of the MFF material also facilitated charge transfer. Both the CoN/Co₄N@C and Co₄N/CoN@C-P electrode materials contained Co₄N and CoN heterostructures; however, the plasma treatment significantly increased the Co₄N content in the heterostructure, which was due to the strong reduction ability of the high-energy electrons generated in the plasma. Moreover, bombardment by high-energy Ar ions rendered the material surface rougher, exposing more Co_xN active sites—beneficial for rapid charge transfer. Finally, more nitrogen atoms were doped into the carbon in Co₄N/CoN@C-P, enhancing the contact between the electrode material and the electrolyte, improving the conductivity of the carbon and thus enhancing the electrochemical charge transfer, further improving the electrochemical performance of the Co₄N/CoN@C-P material. This research demonstrates that plasma engineering of metal–nitride heterostructures derived from MOFs can effectively enhance electrochemical performance, thus providing valuable insights into the controllable preparation of other high-performance electrochemical materials.

Supplementary Materials: The following supporting information can be downloaded at: <https://www.mdpi.com/article/10.3390/ma17143529/s1>. Figure S1: XRD patterns of Co₄N/CoN@C-P (Ar) and Co₄N@C-P (N₂) prepared at 40 Pa, 300 W and discharge time of 6 min; Figure S2: Electrochemical performance for different discharge atmosphere at a fixed power of 300 W and discharge time of 6 min, with different gas pressures of 20, 40, and 60 Pa. (a) CV curves at 10 mV·s⁻¹, (b) GCD curves at 1 A·g⁻¹, (c) EIS curves of Co₄N@C-P(N₂); (d) CV curves at 10 mV·s⁻¹, (e) GCD curves at 1 A·g⁻¹, (f) EIS curves of Co₄N/CoN@C-P(Ar); Figure S3: Electrochemical performance of Co₄N/CoN@C-P(Ar) prepared at 300 W and 40 Pa, with different discharge time of 2, 4, 6, and 8 min. (a) CV curves at 10 mV·s⁻¹; (b) GCD curves at 1 A·g⁻¹; (c) EIS curves; Figure S4: Electrochemical performance of Co₄N/CoN@C-P(Ar) prepared at 40 Pa and discharge time of 6 min, with different discharge powers of 200, 250, 300, and 350 W. (a) CV curves at 10 mV·s⁻¹; (b) GCD curves at 1 A·g⁻¹; (c) EIS curves. Table S1: Equivalent circuit parameters obtained from Nyquist plots of Co-MFF, CoN/Co₄N@C and Co₄N/CoN@C-P; Table S2: The specific surface areas (S_{BET}), pore volumes (V_p), and pore diameters (D_p) of Co-MFF, CoN/Co₄N@C, and Co₄N/CoN@C-P.

Author Contributions: H.L.: Writing—review and editing, supervision, funding acquisition, and project administration. Y.M.: Conceptualization, formal analysis, investigation, methodology, data curation, writing—original draft, software, writing—review and editing. X.Z. (Xulei Zhang): Conceptualization, methodology, validation, writing—review and editing. X.Z. (Xiuling Zhang): Writing—review and editing, supervision. L.D.: Writing—review and editing, funding acquisition, supervision, and project administration. All authors have read and agreed to the published version of the manuscript.

Funding: This work was supported by the National Natural Science Foundation of China (Grant Nos. 12005031, 52077024, 21773020, and 12275041), Xingliao Talents Program (Grant Nos. 2022RJ16 and XLYC2203147), the Interdisciplinary project of Dalian University (Grant No. DLUXK-2023-QN-001), and Postgraduate Education Reform Project of Liaoning Province (Grant No. LNYJG2024335).

Institutional Review Board Statement: Not applicable.

Informed Consent Statement: Not applicable.

Data Availability Statement: The original contributions presented in the study are included in the article/Supplementary Materials, further inquiries can be directed to the corresponding author.

Conflicts of Interest: Author Xulei Zhang was employed by the company Sunstone Energy Co., Ltd. The remaining authors declare that the research was conducted in the absence of any commercial or financial relationships that could be construed as a potential conflict of interest.

References

1. Karthikeyan, S.; Narenthiran, B.; Sivanantham, A.; Bhatlu, L.D.; Maridurai, T. Supercapacitor: Evolution and review. *Mater. Today Proc.* **2021**, *46*, 3984–3988. [[CrossRef](#)]
2. Molahalli, V.; Chaithrashree, K.; Singh, M.K.; Agrawal, M.; Krishnan, S.G.; Hegde, G. Past decade of supercapacitor research—Lessons learned for future innovations. *J. Energy Storage* **2023**, *70*, 108062. [[CrossRef](#)]
3. Reece, R.; Lekakou, C.; Smith, P.A. A High-Performance Structural Supercapacitor. *ACS Appl. Mater. Interfaces* **2020**, *12*, 25683–25692. [[CrossRef](#)] [[PubMed](#)]
4. Şahin, M.; Blaabjerg, F.; Sangwongwanich, A. A Comprehensive Review on Supercapacitor Applications and Developments. *Energies* **2022**, *15*, 674. [[CrossRef](#)]
5. Adalati, R.; Sharma, M.; Sharma, S.; Kumar, A.; Malik, G.; Boukherroub, R.; Chandra, R. Metal nitrides as efficient electrode material for supercapacitors: A review. *J. Energy Storage* **2022**, *56*, 105912. [[CrossRef](#)]
6. Mukhiya, T.; Tiwari, A.P.; Chhetri, K.; Kim, T.; Dahal, B.; Muthurasu, A.; Kim, H.Y. A metal–organic framework derived cobalt oxide/nitrogen-doped carbon nanotube nanotentacles on electrospun carbon nanofiber for electrochemical energy storage. *Chem. Eng. J.* **2021**, *420*, 129679. [[CrossRef](#)]
7. Choi, C.; Ashby, D.S.; Butts, D.M.; DeBlock, R.H.; Wei, Q.; Lau, J.; Dunn, B. Achieving high energy density and high power density with pseudocapacitive materials. *Nat. Rev. Mater.* **2019**, *5*, 5–19. [[CrossRef](#)]
8. Hu, M.; Zhang, H.; Hu, T.; Fan, B.; Wang, X.; Li, Z. Emerging 2D MXenes for supercapacitors: Status, challenges and prospects. *Chem. Soc. Rev.* **2020**, *49*, 6666–6693. [[CrossRef](#)]
9. Simon, P.; Gogotsi, Y.; Dunn, B. Where Do Batteries End and Supercapacitors Begin? *Science* **2014**, *34*, 1210–1211. [[CrossRef](#)]
10. Baig, M.M.; Khan, M.A.; Gul, I.H.; Rehman, S.U.; Shahid, M.; Javaid, S.; Baig, S.M. A Review of Advanced Electrode Materials for Supercapacitors: Challenges and Opportunities. *J. Electron. Mater.* **2023**, *52*, 5775–5794. [[CrossRef](#)]
11. Song, A.; Song, S.; Duanmu, M.; Tian, H.; Liu, H.; Qin, X.; Shao, G.; Wang, G. Recent Progress of Non-Noble Metallic Heterostructures for the Electrocatalytic Hydrogen Evolution. *Small Sci.* **2023**, *3*, 2300036. [[CrossRef](#)]

12. Pham, T.; Forrest, K.A.; Space, B.; Eckert, J. Dynamics of H₂ adsorbed in porous materials as revealed by computational analysis of inelastic neutron scattering spectra. *Phys. Chem. Chem. Phys.* **2016**, *18*, 17141–17158. [[CrossRef](#)]
13. Yang, J.; Ma, Z.; Gao, W.; Wei, M. Layered Structural Co-Based MOF with Conductive Network Frames as a New Supercapacitor Electrode. *Chem. Eur. J.* **2016**, *23*, 631–636. [[CrossRef](#)] [[PubMed](#)]
14. Akkinepally, B.; Kumar, G.D.; Reddy, I.N.; Rao, H.J.; Nagajyothi, P.C.; Allothman, A.A.; Alqahtani, K.N.; Hassan, A.M.; Javed, M.S.; Shim, J. Investigation of Supercapacitor Electrodes Based on MIL-101(Fe) Metal-Organic Framework: Evaluating Electrochemical Performance through Hydrothermal and Microwave-Assisted Synthesis. *Crystals* **2023**, *13*, 1547. [[CrossRef](#)]
15. Senthil, R.A.; Osman, S.; Pan, J.; Liu, X.; Wu, Y. Recent progress on porous carbon derived from Zn and Al based metal-organic frameworks as advanced materials for supercapacitor applications. *J. Energy Storage* **2021**, *44*, 103263. [[CrossRef](#)]
16. Yue, L.; Chen, L.; Wang, X.; Lu, D.; Zhou, W.; Shen, D.; Yang, Q.; Xiao, S.; Li, Y. Ni/Co-MOF@aminated MXene hierarchical electrodes for high-stability supercapacitors. *Chem. Eng. J.* **2023**, *451*, 138687. [[CrossRef](#)]
17. Lan, M.; Wang, X.; Zhao, R.; Dong, M.; Fang, L.; Wang, L. Metal-organic framework-derived porous MnNi₂O₄ microflower as an advanced electrode material for high-performance supercapacitors. *J. Alloys Compd.* **2020**, *821*, 153546. [[CrossRef](#)]
18. Li, Z.; Ren, J.; Bu, J.; Wang, L.; Shi, W.; Pan, D.; Wu, M. Carbonated MOF-based graphene hydrogel for hierarchical all-carbon supercapacitors with ultra-high areal and volumetric energy density. *J. Electroanal. Chem.* **2020**, *876*, 114489. [[CrossRef](#)]
19. Ren, J.; Huang, Y.; Zhu, H.; Zhang, B.; Zhu, H.; Shen, S.; Tan, G.; Wu, F.; He, H.; Lan, S.; et al. Recent progress on MOF-derived carbon materials for energy storage. *Carbon Energy* **2020**, *2*, 176–202. [[CrossRef](#)]
20. Chen, Z.; Song, Y.; Cai, J.; Zheng, X.; Han, D.; Wu, Y.; Zang, Y.; Niu, S.; Liu, Y.; Zhu, J.; et al. Tailoring the d-Band Centers Enables Co₄N Nanosheets to Be Highly Active for Hydrogen Evolution Catalysis. *Angew. Chem. Int. Ed.* **2018**, *57*, 5076–5080. [[CrossRef](#)]
21. Lu, M.; Chen, D.; Wang, B.; Li, R.; Cai, D.; Tu, H.; Yang, H.; Zhang, Y.; Han, W. Boosting alkaline hydrogen evolution performance of Co₄N porous nanowires by interface engineering of CeO₂ tuning. *J. Mater. Chem. A* **2021**, *9*, 1655–1662. [[CrossRef](#)]
22. Ouyang, T.; Cheng, K.; Gao, Y.; Kong, S.; Ye, K.; Wang, G.; Cao, D. Molten salt synthesis of nitrogen doped porous carbon: A new preparation methodology for high-volumetric capacitance electrode materials. *J. Mater. Chem. A* **2016**, *4*, 9832–9843. [[CrossRef](#)]
23. Didziulis, S.V.; Butcher, K.D.; Perry, S.S. Small cluster models of the surface electronic structure and bonding properties of titanium carbide, vanadium carbide, and titanium nitride. *Inorg. Chem.* **2003**, *42*, 7766–7781. [[CrossRef](#)] [[PubMed](#)]
24. Calais, J.L. Band structure of transition metal compounds. *Adv. Phys.* **2006**, *26*, 847–885. [[CrossRef](#)]
25. Dong, S.; Chen, X.; Zhang, X.; Cui, G. Nanostructured transition metal nitrides for energy storage and fuel cells. *Coord. Chem. Rev.* **2013**, *257*, 1946–1956. [[CrossRef](#)]
26. Xie, J.; Xie, Y. Transition Metal Nitrides for Electrocatalytic Energy Conversion: Opportunities and Challenges. *Chem. Eur. J.* **2015**, *22*, 3588–3598. [[CrossRef](#)] [[PubMed](#)]
27. Gao, B.; Li, X.; Ding, K.; Huang, C.; Li, Q.; Chu, P.K.; Huo, K. Recent progress in nanostructured transition metal nitrides for advanced electrochemical energy storage. *J. Mater. Chem. A* **2019**, *7*, 14–37. [[CrossRef](#)]
28. Zheng, D.; Yu, L.; Liu, W.; Dai, X.; Niu, X.; Fu, W.; Shi, W.; Wu, F.; Cao, X. Structural advantages and enhancement strategies of heterostructure water-splitting electrocatalysts. *Cell Rep. Phys. Sci.* **2021**, *2*, 100443. [[CrossRef](#)]
29. Zhang, H.; Maijenburg, A.W.; Li, X.; Schweizer, S.L.; Wehrspohn, R.B. Bifunctional Heterostructured Transition Metal Phosphides for Efficient Electrochemical Water Splitting. *Adv. Funct. Mater.* **2020**, *30*, 2003261. [[CrossRef](#)]
30. Strasser, P.; Koh, S.; Anniyev, T.; Greeley, J.; More, K.; Yu, C.; Liu, Z.; Kaya, S.; Nordlund, D.; Ogasawara, H.; et al. Lattice-strain control of the activity in dealloyed core-shell fuel cell catalysts. *Nat. Chem.* **2010**, *2*, 454–460. [[CrossRef](#)]
31. Du, X.; Huang, J.; Zhang, J.; Yan, Y.; Wu, C.; Hu, Y.; Yan, C.; Lei, T.; Chen, W.; Fan, C.; et al. Modulating Electronic Structures of Inorganic Nanomaterials for Efficient Electrocatalytic Water Splitting. *Angew. Chem. Int. Ed.* **2019**, *58*, 4484–4502. [[CrossRef](#)] [[PubMed](#)]
32. Tang, Y.; Dong, L.; Wu, H.B.; Yu, X.-Y. Tungstate-modulated Ni/Ni(OH)₂ interface for efficient hydrogen evolution reaction in neutral media. *J. Mater. Chem. A* **2021**, *9*, 1456–1462. [[CrossRef](#)]
33. Di, L.; Zhang, J.; Zhang, X.; Wang, H.; Li, H.; Li, Y.; Bu, D. Cold plasma treatment of catalytic materials: A review. *J. Phys. D Appl. Phys.* **2021**, *54*, 333001. [[CrossRef](#)]
34. Gururani, P.; Bhatnagar, P.; Bisht, B.; Kumar, V.; Joshi, N.C.; Tomar, M.S.; Pathak, B. Cold plasma technology: Advanced and sustainable approach for wastewater treatment. *Environ. Sci. Pollut. Res.* **2021**, *28*, 65062–65082. [[CrossRef](#)] [[PubMed](#)]
35. Kang, Q.; Wang, C.; Niu, F.; Zhou, S.; Xu, J.; Tian, Y. Single-crystalline SiC integrated onto Si-based substrates via plasma-activated direct bonding. *Ceram. Int.* **2020**, *46*, 22718–22726. [[CrossRef](#)]
36. Racka-Szmidt, K.; Stonio, B.; Żelazko, J.; Filipiak, M.; Sochacki, M. A Review: Inductively Coupled Plasma Reactive Ion Etching of Silicon Carbide. *Materials* **2021**, *15*, 123. [[CrossRef](#)]
37. Seok, H.; Shin, D.; Kim, H.U.; Kim, T. Flexible Sensor Platform: Nano-grain of 2D Heterostructure by Cold-Plasma. In Proceedings of the 2022 IEEE International Symposium on Medical Measurements and Applications (MeMeA), Messina, Italy, 22–24 June 2022; pp. 1–6.
38. Hong, J.; Park, S.J.; Kim, S. Synthesis and electrochemical characterization of nanostructured Ni-Co-MOF/graphene oxide composites as capacitor electrodes. *Electrochim. Acta* **2019**, *311*, 62–71. [[CrossRef](#)]
39. Xiong, D.; He, X.; Liu, X.; Gong, S.; Xu, C.; Tu, Z.; Wu, D.; Wang, J.; Chen, Z. 1D/3D Heterogeneous Assembling Body of Cobalt Nitrides for Highly Efficient Overall Hydrazine Splitting and Supercapacitors. *Small* **2023**, *20*, e2306100. [[CrossRef](#)]

40. Jayaramulu, K.; Horn, M.; Schneemann, A.; Saini, H.; Bakandritsos, A.; Ranc, V.; Petr, M.; Stavila, V.; Narayana, C.; Scheibe, B.; et al. Covalent Graphene-MOF Hybrids for High-Performance Asymmetric Supercapacitors. *Adv. Mater.* **2020**, *33*, 2004560. [[CrossRef](#)]
41. Xiong, D.; Lu, C.; Chen, C.; Wang, J.; Chen, J.; Yi, F.Y.; Ma, X. The design and fabrication of ultrahigh-performance supercapacitor electrodes from bimetallic PBA/Ni(OH)₂/Co₃O₄/NF quaternary hybrid nanocomposites. *Mater. Chem. Front.* **2021**, *5*, 1388–1397. [[CrossRef](#)]
42. Hu, L.; Sun, K.; Peng, Q.; Xu, B.; Li, Y. Surface active sites on Co₃O₄ nanobelt and nanocube model catalysts for CO oxidation. *Nano Res.* **2010**, *3*, 363–368. [[CrossRef](#)]
43. Zhang, L.; Song, H.; Xu, G.; Wang, W.; Yang, L. MOFs derived mesoporous Co₃O₄ polyhedrons and plates for CO oxidation reaction. *J. Solid State Chem.* **2019**, *276*, 87–92. [[CrossRef](#)]
44. Duan, X.; Chen, J.; Xiang, X.; Zhou, A.; Xiao, J.; Wen, J.; Wang, S. Investigation of flow and heat transfer performances of novel water electrolyzer with conductive particles. *Int. J. Hydrogen Energy* **2024**, *61*, 188–196. [[CrossRef](#)]
45. Fan, L.; Zhao, J.; Jing, F.; Ma, Z.; Fan, Y.; Qin, X.; Shao, G. Fabrication of oxygen-vacancy abundant MnO₂ nanowires@NiMn_xO_{y-δ} nanosheets core-shell heterostructure for capacity supercapacitors. *J. Energy Storage* **2022**, *52*, 104845. [[CrossRef](#)]
46. Song, J.; He, B.; Shen, H.; Wu, Z.; Yu, J.; Lei, W.; Xia, X.; Du, P.; Hao, Q. Rational Design of a ZIF-67/Cobalt-Glycolate Heterostructure with Improved Conductivity for High Cycling Stability and High-Capacity Lithium Storage. *ChemElectroChem* **2021**, *8*, 2431–2441. [[CrossRef](#)]
47. Zhang, X.; Liu, Z.; Wei, X.; Ali, S.; Lang, J.; Yang, B.; Hu, R.; Qi, J.; Yan, X. Unraveling the improved lithium-storage mechanism by interfacial engineering based on metallic MoS₂/MoN heterostructure. *J. Alloys Compd.* **2023**, *966*, 171282. [[CrossRef](#)]
48. Ray, C.; Lee, S.C.; Jin, B.; Kundu, A.; Park, J.H.; Chan Jun, S. Conceptual design of three-dimensional CoN/Ni₃N-coupled nanograsses integrated on N-doped carbon to serve as efficient and robust water splitting electrocatalysts. *J. Mater. Chem. A* **2018**, *6*, 4466–4476. [[CrossRef](#)]
49. Xu, Z.; Li, W.; Yan, Y.; Wang, H.; Zhu, H.; Zhao, M.; Yan, S.; Zou, Z. In-Situ Formed Hydroxide Accelerating Water Dissociation Kinetics on Co₃N for Hydrogen Production in Alkaline Solution. *ACS Appl. Mater. Interfaces* **2018**, *10*, 22102–22109. [[CrossRef](#)] [[PubMed](#)]
50. Ouyang, B.; Sun, C.; Wang, X.; Xu, J.; Cao, Y.; Wu, F.; Singh Rawat, R.; Zhu, J.; Kan, E. Structural control of heterostructured Co₃N-Co nano-corals for boosting electrocatalytic hydrogen evolution based on insulator-confined plasma engineering. *Chem. Eng. J.* **2023**, *466*, 143211. [[CrossRef](#)]
51. Zhang, Y.; Ouyang, B.; Xu, J.; Jia, G.; Chen, S.; Rawat, R.S.; Fan, H.J. Rapid Synthesis of Cobalt Nitride Nanowires: Highly Efficient and Low-Cost Catalysts for Oxygen Evolution. *Angew. Chem. Int. Ed.* **2016**, *55*, 8670–8674. [[CrossRef](#)]
52. Ghosh, S.; Barg, S.; Jeong, S.M.; Ostrikov, K. Heteroatom-Doped and Oxygen-Functionalized Nanocarbons for High-Performance Supercapacitors. *Adv. Energy Mater.* **2020**, *10*, 2001239. [[CrossRef](#)]
53. Xiao, K.; Ding, L.X.; Liu, G.; Chen, H.; Wang, S.; Wang, H. Freestanding, Hydrophilic Nitrogen-Doped Carbon Foams for Highly Compressible All Solid-State Supercapacitors. *Adv. Mater.* **2016**, *28*, 5997–6002. [[CrossRef](#)] [[PubMed](#)]
54. Zhang, E.; Wu, Y.-C.; Shao, H.; Klimavicius, V.; Zhang, H.; Taberna, P.L.; Grothe, J.; Buntkowsky, G.; Xu, F.; Simon, P.; et al. Unraveling the Capacitive Charge Storage Mechanism of Nitrogen-Doped Porous Carbons by EQCM and ssNMR. *J. Am. Chem. Soc.* **2022**, *144*, 14217–14225. [[CrossRef](#)] [[PubMed](#)]

Disclaimer/Publisher's Note: The statements, opinions and data contained in all publications are solely those of the individual author(s) and contributor(s) and not of MDPI and/or the editor(s). MDPI and/or the editor(s) disclaim responsibility for any injury to people or property resulting from any ideas, methods, instructions or products referred to in the content.